Agulhas ring transport efficiency from combined satellite altimetry and Argo profiles

Francesco Nencioli[1], **Giorgio Dall'Olmo**[1,2] **and Graham D. Quartly**[1]

[1]Plymouth Marine Laboratory, Plymouth, UK

[2]National Centre for Earth Observation, Plymouth, UK

Key Points:

- Main eddy volume losses due to eddy-ridge interactions
- Eddy waters continuously exchanged along eddy tracks
- Volume losses and water exchanges not uniform with depth

Corresponding author: Francesco Nencioli, fne@pml.ac.uk

Abstract

Agulhas rings are one of the main processes contributing to the westward transport of Agulhas leakage water across the South Atlantic basin. Here, we quantified the water transported and exchanged by three Agulhas rings by combining remote-sensing altimetry and in-situ Argo observations. Satellite velocities showed that two of the eddies formed within the Cape Basin west of South Africa at the beginning of 2013 and reached the Mid-Atlantic Ridge by the end of 2014. There, they merged forming the third eddy which dissipated a year later when it approached the Brazilian continental shelf. Eddy structure reconstructed from Argo profiles showed that the eddies were at least 1500-m deep and that their dynamics was strongly affected by the two open-ocean ridges encountered along their path. Between the ridges, eddy volumes were mostly conserved, but waters were continuously exchanged. During eddy dissipation, volume losses and water exchanges were more pronounced at depth. These findings highlight the importance of combining surface with in-situ information to accurately represent Agulhas ring transport and exchanges. Overall, the eddies transported roughly 0.5×10^{13} m^3 of water from the Cape Basin to west of 30°W in a 3-year span. Lagrangian diagnostics indicated that, after an initial period of instability, the surface waters exchanged by the eddies along their tracks dispersed roughly in the same direction as the eddies, albeit at a much slower rate. These results further confirm that Agulhas eddies are the most efficient process for westward transport across the South Atlantic basin.

1 Introduction

The Agulhas system is characterized by warm saline waters that leak from the Indian to the Atlantic Ocean [*De Rutijer et al.*, 1999]. This Agulhas leakage is key for the global circulation since it feeds the surface branch of the South Atlantic meridional overturning circulation (SAMOC) [*Beal et al.*, 2011]. One of the main processes contributing to the westward transport of the leaked waters across the whole South Atlantic basin are Agulhas rings [e.g. *Gordon and Haxby*, 1990; *Goni et al.*, 1997]. These rings are among the largest and most coherent eddies in the world [*Gordon and Haxby*, 1990; *Olson*, 1991], with diameters of hundreds of km and life spans of more than 2 years. Due to their importance, the quantification of the transport associated with these eddies has been the focus of several studies [e.g. *Schouten et al.*, 2000; *van Sebille et al.*, 2010; *Souza et al.*, 2011]. In recent years, these estimates have been further refined with the emergence of

Lagrangian techniques capable of detecting coherent mesoscale eddies [*Haller and Beron-Vera*, 2013, 2014]. Compared with traditional Eulerian eddy-detection [e.g. *Chaigneau et al.*, 2008; *Nencioli et al.*, 2010; *Chelton et al.*, 2011], studies based on these novel techniques can identify eddies capable of transporting water within their core with no noticeable leakage [*Wang et al.*, 2015, 2016; *Froyland et al.*, 2015]. Thus, these Lagrangian studies can provide more accurate estimates of the associated eddy-transport. However, since the detection is usually applied to satellite-based velocity fields, such quantifications are based on surface information only, and eddy volumes can only be derived using a-priori assumptions about the vertical structure of the eddies.

In-situ profiles of temperature and salinity to study the vertical structure of, and transport associated with, mesoscale eddies can be obtained on a quasi-daily basis from autonomous Argo floats [*Argo*, 2000]. Although not specifically designed for targeting mesoscale processes, Argo observations have been used more and more frequently in synergy with remote sensing measurements in eddy-focused studies both at the basin [*Qiu and Chen*, 2005; *Chaigneau et al.*, 2011; *Lyman and Johnson*, 2015; *Amores et al.*, 2017], and the global scales [*Dong et al.*, 2014; *Zhang et al.*, 2014]. All these studies have used the profiles collected over a large number of eddies to investigate average eddy characteristics over a given region or period of time. Thus, while successful for the statistical characterization of mesoscale activity, these synergistic approaches remain untested for the direct characterization of individual mesoscale features.

Here, we will combine for the first time (to the best of our knowledge) in-situ Argo observations and remote-sensing altimetry to study the life cycle of specific Agulhas eddies. In particular, the synergistic approach will be used to investigate the temporal evolution of their characteristics and associated transport as they traveled across the South Atlantic Ocean. Altimetry will be used to identify and track the three eddies; Argo observations will provide in-situ evidence of the induced transport and exchanges. Furthermore, in-situ profiles will be used to reconstruct the vertical structure of the eddies, so that no a-priori assumptions will be required. Therefore, it will be possible to investigate how eddy-induced transport and exchanges vary with depth. Our results will be compared with previous studies based on coherent-eddy detection, to assess the validity of some of the assumptions at the base of those studies. As Agulhas-ring contribution to the SAMOC does not depend only on the total amount of water transported across the South Atlantic basin, but also on where and when losses occur [*Froyland et al.*, 2015], the fate of the exchanged water will also be investigated.

2 Material and Methods

2.1 Altimetry-based Eddy Detection

Eddies were detected from global multi-satellite gridded geostrophic velocities (1/4° resolution) from the SSALTO/DUACS "all-sat-merged" data set [*SSALTO/DUACS User Handbook*, 2016]. Eddy detection was based on the automated algorithm described in *Nencioli et al.* [2010], which identifies and tracks eddies following 4 constraints on the geometry of the velocity field. The algorithm was applied with detection parameters a=4 and b=3, and tracking radius r=5 (full details in *Nencioli et al.* [2010]) to the daily-velocity anomalies from 1 January 2013 to 31 December 2016 over the region 45°S to 5°S, and 50°W to 32°E. As in *Liu et al.* [2012] and *Amores et al.* [2013], the original SSALTO/DUACS velocities were linearly interpolated to a 1/8° grid to improve the detection performance.

2.2 Argo and BGC-Argo Profiles

Once eddy centers were identified from satellite altimetry, vertical profiles from the Argo dataset [*Argo*, 2000] were used to reconstruct their 3-dimensional structure. For this study, we selected profiles collected between 0 and 400 km from the identified eddy centers. These consisted of 728 profiles collected by 46 different floats.

For each profile, T and S were converted to absolute salinity (S_A) and conservative temperature (Θ), which were used to compute potential density (ρ_θ) referenced to the sea surface via the Thermodynamic Equation Of Seawater - 2010 (TEOS-10; http://www.teos-10.org/). Following *Gray and Riser* [2014], the ρ_θ profiles were interpolated to the standard depth levels of the World Ocean Atlas 2013 version 2 (5 m-resolution for 0-100 m depth, 25 m for 100-500 m depth and 50 m for 500-1500 m depth (see https://www.nodc.noaa.gov/OC5/woa13/) using a monotone cubic Hermite interpolation [*Fritsch and Carlson*, 1980]. Profiles that contained ρ_θ inversion $\leq$-0.02 kg m^{-3} for successive (deeper) bins were further corrected by removing that portion of the profile and re-interpolating [*Gray and Riser*, 2014]. Finally, the shallowest available measurement of a profile was extended to the surface if it was collected at depth $\leq$15 m, or within the upper mixed layer, defined by shallowest depth ≤200 m and ρ_θ variation at the successive bin ≤0.03 kg m^{-3} [*de Boyer Montégut et al.*, 2004].

Our analysis also included observations from a Biogeochemical (BGC)-Argo float (WMO number 3901496), deployed in the South-western Atlantic on 20 October 2014. BGC-Argo floats are analogous to the Argo ones, but they are equipped with additional sensors for measuring various biogeochemical variables. The float provided vertical profiles every 5 days from a parking depth of 1000 m.

2.3 Three-Dimensional Eddy Reconstruction

To reconstruct the 3-dimensional structure (hereafter 3D) of the eddies, we adapted the approach described in *Zhang et al.* [2013, 2014]. Since our analysis focused on specific mesoscale eddies, the approach was applied on a temporal rather than a regional basis. We used Argo data from Section 2.2 to compute vertical profiles of pressure anomaly, P', at various radial distances from the identified eddy centers. The profiles were then grouped based on a 3-month window centered over successive months. Radial sections of a given eddy over successive months were reconstructed by fitting the observations from each 3-month window with an analytical radial function with depth-varying amplitude. Sensitivity analyses showed that shorter window widths, despite reducing overlapping (and, hence, time-series smoothing), did frequently provide too few observations along an eddy radius for a robust fit of the analytical radial function. Monthly time series of the 3D structure of each eddy were reconstructed assuming mesoscale eddies to be radially symmetric with no tilt in their vertical axis.

Following *Zhang et al.* [2014], profiles of P' were computed by upward integration of Argo density anomalies, ρ'_θ, from a depth of 2000 m, chosen as the level of no motion:

$$P'(r,z)_{Argo} = -\int_{-2000}^{z} g\rho'_\theta(r,z')_{Argo}dz' \quad (1)$$

where r is the distance of a given profile from the eddy center and g is the gravitational acceleration. $\rho'_\theta(r,z)_{Argo}$ was obtained as the difference between each observed profile, $\rho_\theta(r,z)_{Argo}$, and the mean from those collected between 300 and 400 km, $\bar{\rho}_\theta(z)_{Argo}$. The latter are representative of the background conditions outside the eddies, since they were collected beyond the maximum eddy radius observed by *Chelton et al.* [2011], as well as the region of opposite signed anomaly around the eddy identified by *Zhang et al.* [2013]. As the 2000-m depth was assumed as the level of no motion, $\rho'_\theta(r,-2000)$ was set to 0 in each profile. To maximize the number of P' profiles available for the analysis, incomplete profiles of ρ'_θ which extended to at least 1000 m depth (more than half of the WOA water column) were interpolated to 2000 m using the same monotone cubic Hermite interpolation as for ρ_θ in section 2.2. These consisted of 98 of the 728 profiles (37 deeper than 1200 m, 61 between 1000 and 1200 m depth). On the other hand, 24 profiles were not retained for the analysis because they were either too shallow or characterized by anomalous features (e.g. non-monotonic depth, unrealistic values of ρ'_θ or persisting inversions after the correction).

For each time-window, radial sections of P' were reconstructed by fitting the observations with the Gaussian analytical function

$$P'(r, z_i)_{Fit} = P'_0(z_i)\exp\left(-\frac{r^2}{2R_0(z_i)^2}\right) \tag{2}$$

where $P'_0(z_i)$, the pressure anomaly at the eddy center, and $R_0(z_i)$, indicator of the width of the Gaussian bell, were the two parameters to be determined. The Gaussian profile was preferred to the radial function used in *Zhang et al.* [2013], since it was found to be less sensitive to the P' values outside or at the edge of the eddy, and thus more reliable especially for the deeper sections, usually characterized by lower values of P'_0 at the eddy center. The function was fitted independently for each depth-level z_i. This depth-resolved fitting resulted in a more accurate reconstruction of the vertical profile of P' compared with the analytical vertical function proposed by *Zhang et al.* [2013], which, in our case, tended to overestimate P' in the upper mixed layer and underestimate it at its subsurface maximum (not shown). The fit was obtained through a non-linear least square minimization using the Trust Region Reflective algorithm [*Branch et al.*, 1999] (function curve_fit.py from the scipy.optimize library: https://docs.scipy.org/doc/scipy/reference/generated/scipy.optimize.curve_fit.html), with initial values of 0 and 100 for $P'_0(z_i)$ and $R_0(z_i)$, respectively, and bound values 0 and ∞ for both parameters.

Once the vertical profiles of P'_0 and R_0 were determined, the full 3D field, $P'(r, z)$, was reconstructed within 300 km from the eddy center using equation 2 and assuming radial symmetry.

Not all the reconstructed sections were retained in the analysis. Despite grouping Argo profiles within 3-month windows, some months were characterized by insufficient observations, especially within the first tens of km from the eddy center. These observations close to the eddy center are particularly important to reliably fit the Gaussian profile.

As $R_0(z_i)$ usually varied between 50 and 100 km, sections with at least one profile within 50 km from the eddy center were always retained. On the other hand, sections with no profiles within 50 km, but at least one within 100 km from the center, were retained only if the coefficient of determination (used as indicator for the goodness of the radial fit) obtained using the observations within 200 km from the center (outer limit of the Gaussian profile) was ≥ 0.7. Sections reconstructed with no profiles within 100 km from the eddy center were assumed unreliable and discarded (see Section 3).

To quantify the volume of the eddy, we used a modified version of the approach from *Zhang et al.* [2014, 2017]: instead of potential vorticity, eddy boundaries were defined based on closed contours of absolute vorticity resulting in more conservative estimates of eddy dimensions (see Appendix A:). The total volume of the eddy was then obtained as the sum of the volumes at each depth level from 0 to 1500 m using the estimated eddy radii. The associated relative error is estimated to be around 20% [*Zhang et al.*, 2014].

2.4 Particle dispersion

The Lagrangian analysis was based on the LAgrangian Manifolds and Trajectories Analyser (LAMTA) described in *van Sebille et al.* [2018] and already used to support, among others, experiments in the NW Mediterranean [*Nencioli et al.*, 2011], and southern Indian Ocean [*d'Ovidio et al.*, 2015]. The analysis used SSALTO/DUACS total velocities for the advection within the upper mixed layer. At the beginning of each month, particles were released within 150 km from the eddy centers with a spatial resolution of 1/12° (~8 km at 30°S), and then advected both backward and forward in time for 180 days. The advection is performed with Runge-Kutta fourth-order scheme and a 6-hour time step, with the velocity field interpolated bi-linearly in space and linearly in time.

3 Results

Our study stemmed from the BGC-Argo float observations. The vertical profiles between July and August 2015, when the float was between 28 and 25°W and 24 to 22°S, were characterized by strong anomalies in T, S and oxygen down to 1000 m depth (Figure 1). To better understand the role played by local temporal variability and horizontal advection in determining such anomalies, we first investigated the evolution of the surface geostrophic velocities in the region around the BGC-Argo float. Successive daily snapshots of the surface velocity field showed that the observed anomalies were associated with the passage of a large anticyclonic mesoscale eddy (Figure 2).

To characterize origin, pathway and age of the eddy, we applied the automated eddy detection and tracking over a broader region spanning the whole width of the South Atlantic (Figure 3). This analysis showed that the eddy first formed on 10 October 2014 at 27.63°S-12.75°W, and dissipated on 29 December 2015 at 21.0°S-34.75°W. The eddy spawned from the merging of two Agulhas rings immediately west of the Mid-Atlantic Ridge. One of the rings formed on 9 August 2013 at 33.38°S-10.25°E, the other was already present on 1 January 2013 at 32.63°S-9.13°E. We will refer to the three eddies as *AN1* (the northern Agulhas ring), *AS2* (the southern Agulhas ring) and *B12* (the eddy originated from the merging of the two). The eddies shared similar characteristics, with average radii of 73±11, 70±9 and 67±11 km, and translational speeds of 7.2±4.7, 5.5±4.8 and 7.8±5.0 cm s^{-1}, respectively, in line with values observed by *Chelton et al.* [2011] at similar latitudes.

The eddy tracks suggested that the anomaly observed by the BGC-Argo float could potentially be associated with waters trapped within the eddies in the eastern South Atlantic and transported to the west as the eddies crossed the basin over a 3-year span. Since eddies detected via Eulerian methods cannot be automatically associated with coherent advection of water [*Beron Vera et al.*, 2013], we analysed in-situ Argo observation to infer if such transport occurred. The time-series of Argo profiles collected within 100 km from the *AN1* and *B12* eddy centers are shown in Figure 4. *T* and *S* profiles from eddy *AN1* showed that below 200 m depth the eddy was characterized by warmer and saltier waters compared with the background conditions observed by the BGC-Argo float. Despite some variability, the profiles seemed to remain around the same values throughout the eddy lifetime. The eddy was characterized by spicier waters (with spice computed following *McDougall and Krzysik* [2015]) throughtout the upper 1000 m and showed a much reduced stratification between 200 and 400 m depth (see supporting information Figures 3 and 4). In the upper layer, lower temperatures than the surrounding waters (see also supporting information Figure 7) are consistent with the meridional heat flux by Agulhas rings observed in *Souza et al.* [2011], as well as with the enhanced air-sea interaction by southern eddies reported by *Frenger et al.* [2015]. For eddy *B12*, values of *T* and *S* below 200 m depth have initial values in line with the ones observed within eddy *AN1*, indicating that the observed anomaly (or at least a part of it) was inherited by the eddy. Thus, in-situ Argo profiles support our initial interpretation that the eddies effectively trapped and transported the same water mass. Eddy water trapping and transport are further supported by the eddy signatures on 8-day composite maps of ocean colour and sea surface temperature (see supporting information Figures 5, 6 and 7) as well as by the analysis of Argo float trajectories. These, in particular, show that a float (WMO number 1901544) trapped within eddy *AN1* (< 100 km from its center) on February 2014 did follow the eddy from $\sim 0°$ to past 25°W, including after its merging with eddy *B12*, and escaped the latter only after August 2015 (see supporting information Figure 8). After eddy *B12* formation, the profiles show a temporal trend towards the observed background values (a decrease of roughly 2.5°C in a year at 400 m depth), indicating that water was exchanged between the eddy interior and its surroundings during the westward migration in the South Atlantic, even before its dissipation.

To investigate the eddy exchanges in more detail, we analysed the temporal variations of the reconstructed 3D structure of these three eddies. The first two sections of eddy *AN1* (September and October 2013) and the last three of eddy *B12* (October to December 2015) were removed from the respective time series due to insufficient contributing profiles (according to the criteria specified in Section 2.3). Due to the persistent lack of observations within the eddy, only the sections reconstructed between December 2013 and April 2014 were retained for eddy *AS2*. The reconstructed radial section of eddy *AN1* for April 2014 is shown as an example in Figure 5. Radial profiles at different depths (bottom panels) showed that the Gaussian function from equation 2 fitted the observations within its core ($\lesssim$150 km) well, but (as already anticipated) did not reproduce the band of negative pressure anomalies around the eddy (roughly between 150 and 250 km). The reconstructed vertical section of $P'(r,z)_{Fit}$ (top left) showed that the eddy core was characterized by a positive anomaly with decreasing values with distance from the eddy center. In the vertical, it was characterized by a subsurface maximum at ~200 m depth, a direct consequence of the typical mode-water eddy structure observed in the density section (top right): density differences were large and negative (lighter water within the eddy than the surrounding) at depth, while positive but weaker in the upper layer. Comparison with the observations showed that our approach returned an accurate reconstruction of the vertical structure of both observed pressure and density fields (top center and right). Although radial sections at each depth level were reconstructed independently, $R_0(z_i)$ did not show large variations with depth (values between 75 and 100 km, not shown) and confirmed that the horizontal structure of P' associated with an eddy is to first order independent of depth, as first observed by *Zhang et al.* [2013].

The time series in Figure 6, top, shows the water exchanged from an eddy to the surroundings due to its progressive loss of trapped volume. The time series of eddy *AN1* showed that as the eddy crossed the Walvis Ridge its volume dropped sharply from 2×10^{13} m^3 to ~1.5×10^{13} m^3. After that, if we exclude the two estimates between 4°W and 7.5°W (discussed at the end of this Section), the eddy volume showed only a moderate decrease, remaining above 1×10^{13} m^3 until the eddy merged into *B12* while crossing the Mid-Atlantic Ridge. Volume estimates for eddy *AS2*, although insufficient to reconstruct the full evolution along the eddy track, indicated analogous characteristics to eddy *AN1* between the two ridges. Eddy *B12* was initially characterized by a volume similar to eddy *AN1* before the Mid-Atlantic Ridge, suggesting that, after the merging of eddies *AN1* and *AS2*, eddy *B12* inherited only half of the volume of the two eddies combined. Backward Lagrangian experiments showed that 51.4% of the water in its mixed layer came from eddy *AS2*, with only 20.4% traceable to eddy *AN1*, and the remaining 28.2% originating from the surrounding waters. (Full animation can be seen at https://www.youtube.com/watch?v=hak7D_WWG6E). This different contribution from the two eddies also explains the colder temperatures of the early profiles within eddy *B12* compared with the late ones within eddy *AN1* shown in Figure 4, bottom. After the ridge, eddy *B12* volume remained between 1.5×10^{13} and 1×10^{13} m^3 until 25°W (corresponding to June 2015) where it showed a sharp decrease to $<0.5 \times 10^{13}$ m^3 as the eddy started to dissipate.

Water losses due to reducing eddy volume are not the only source of exchanges between an eddy and its surroundings. Water can also be exchanged by diffusive-like processes at smaller-scales (compared to the to the reconstructed eddy structure) that induce mixing between waters within and outside the eddy with negligible changes in volume. Since water exchanges modify the water properties within the eddy, the time series of density anomaly at the eddy center was investigated (Figure 6, bottom). The upper 200 m were characterized by marked seasonal variations (see temperature profiles in Figure 4, bottom), indicating that, as observed by *Lehahn et al.* [2011], the mixed layer within the eddies remained strongly influenced by fluxes and vertical mixing associated with the atmospheric forcing. To minimize the impact of the seasonal cycle, we focused on the time series below the seasonal thermocline.

Similarly to the eddy volume, the anomaly amplitude for eddy *AN1* rapidly decreased before the eddy crossed the Walvis Ridge (roughly -0.1 kg m^{-3} month^{-1} at 400 m depth; Figure 6, bottom). Afterwards, it showed a more gradual but steady decrease until the eddy merged. This trend was hidden in Figure 4 (bottom right) by the spatial variability associated with the varying radial distances at which the profiles were collected. However, such variability was removed in Figure 6 by analysing the reconstructed anomalies at the eddy center. Density anomaly values within eddy *AS2*, although insufficient to reconstruct the full evolution along the eddy track, indicated analogous characteristics to eddy *AN1*. The anomalies of eddy *B12* showed similar values as observed for eddy *AN1* before the Mid-Atlantic Ridge (see also temperature profiles in Figure 4, bottom) followed by a steady decrease at all depths until 25°W, despite the volume of eddy *B12* remaining roughly constant. When the eddy began to dissipate and to rapidly lose volume, anomalies at 400 m depth remained roughly constant, whereas at deeper depths density sharply dropped towards the background values.

The two time series suggest that, although mixing across the eddy boundary could be enhanced at times of increased volume losses, it occurred independently of them. Furthermore, as shown by the eddy *B12* time series, the exchanges were not always uniform with depth, especially during eddy decay. Time series of eddy radii at the same depths supported this interpretation (not shown). Although reduced in size, eddy *B12* maintained its core characteristics at 400 m depth beyond 25°W, whereas it rapidly dissipated (eddy radius dropping to ~0) below 800 m, suggesting that the observed decrease in eddy volume occurred non-uniformly with depth during eddy dissipation. Such variations reflect an eddy decay towards a smaller but also shallower structure due to larger deep volume losses. A shallower eddy structure is also consistent with the trajectories of the BGC-Argo float and the two Argo floats (WMO numbers 1901296 and 3901500) which sampled eddy *B12* core (<100 km from its center) after July 2015 (see supporting information Figure 8): they were all influenced by the passage of the eddy, but did not remain trapped within it.

Unlike the volume time series, density anomalies did not show sharp changes between 4° and 7.5°W. Inspection of the two sections reconstructed within those longitudes (corresponding to June and July 2014) showed that although values of $P'_0(z_i)$, the vertical profile of pressure anomaly at the eddy center, were similar to neighboring sections, the derived $R_0(z_i)$ were much broader, implying weaker radial pressure gradients and relative vorticity. Consequently, the largest closed contours of absolute vorticity were much smaller, leading to decreased values for the eddy radii and total volumes. Thus, although there were no clear errors in the fitted sections, these Argo-derived estimates seem anomalous. This is also consistent with the altimetry-based eddy detection which did not show any significant decrease in the surface eddy dimensions. Indeed, it is hard to hypothesize such a sharp decrease in eddy volume (to almost complete eddy dissipation) sustained for successive months but not accompanied by similar variations in density anomalies within the eddy. These anomalous values indicate that the proposed approach still has some limitations that must be investigated and resolved in future studies before the method can be reliably applied for a completely unsupervised analysis of longer eddy time series.

The fate of the exchanged waters at the surface was investigated through the forward Lagrangian experiments described in Section 2.4. Figure 7 (top) shows the final particle positions for six experiments conducted between March 2013 and October 2015. The dispersion patterns identified three distinct regions. The Cape Basin east of the Walvis Ridge (rightmost green particles) was quite chaotic, as already observed in earlier studies based on altimetry data [e.g. *Schouten et al.*, 2000]. Eddies *AN1* and *AS2* retained only a small fraction of the particles initially seeded within their cores. The exchanged particles spread roughly uniformly from west to southeast around the eddies (Figure 7, bottom right). After the two eddies crossed the ridge (rightmost magenta particles), their ability to retain particles drastically increased. Only a small percentage of the exchanged particles was advected northeastward, towards the Angola Basin, or southeastward, back towards the Agulhas region. Most of the exchanged particles continued to be advected northwestward, albeit at a much slower rate than those advected by the eddies. The percentage of westward to northwestward propagating exchanged particles progressively increased after the two eddies merged across the Mid-Atlantic Ridge until eddy *B12* dissipated (middle green and leftmost magenta particles). These results are consistent with the volume time series in Figure 6. Finally, as the eddy dissipated, the particles spread roughly equally to the north and the southwest constrained by the presence of the Brazilian coast.

4 Discussion and Conclusions

The volume transport associated with three Agulhas rings was investigated by synergistically combining altimetry and in-situ Argo profiles. This approach allowed the reconstruction of the 3D structure of the eddies, so that temporal and depth variability of volume transport and exchanges were directly investigated without a-priori assumptions on the vertical eddy structure. Altimetry-based eddy tracking showed that two of the rings (*AN1* and *AS2*) were present within the Cape Basin on January and August 2013. Afterwards, they propagated roughly to the northwest and merged immediately west of the Mid-Atlantic Ridge in October 2014 (with the larger contribution from eddy *AS2*), to form the third eddy (*B12*). The new eddy continued to propagate to the northwest and eventually dissipated in December 2015 in front of the southeastern Brazilian coast. The 3D structure of the eddies was reconstructed on a monthly basis based on a modified version of the approach from *Zhang et al.* [2013, 2014]. Since eddy boundaries were defined based on the largest closed contour of absolute vorticity (η), the resulting estimates of total water volume trapped within the eddy were likely more conservative than those based on potential vorticity (*PV*) (see Appendix A:).

The largest exchanges occurred when the eddies crossed the Walvis and Mid-Atlantic ridges (~0.5 and ~1.0×10^{13} m^3, respectively). Interactions with such topographic features are not surprising given that that the vertical extent of the eddies inferred from the profiles of density anomalies was deeper than 1500 m. The loss of volume induced by such interactions is consistent with results by *Frenger et al.* [2015] who showed that bottom interactions are one of the most important processes to dissipate mesoscale energy in the Southern Ocean. Between the two ridges the eddies showed reduced volume losses ($<0.5 \times 10^{13}$ m^3), as observed in *Froyland et al.* [2015] and *Wang et al.* [2016]. Other studies [*Doglioli et al.*, 2007; *van Sebille et al.*, 2010] have reported larger volume losses. However, they focused on Agulhas rings within the Cape Basin, which is characterized by a strongly chaotic dynamics [*Boebel et al.*, 2003], as also confirmed by our Lagrangian experiments. Numerical results have also confirmed that Agulhas rings tend to stabilize downstream of topographic ridges [*de Steur and van Leeuwen*, 2009]. The ~0.5×10^{13} m^3 of water advected by eddy *B12* west of 30° W corresponds to ~33% of the initial volume of the eddy after the Mid-Atlantic Ridge, and to ~12.5% of the initial combined volume of eddies *AN1* and *AS2* east of the Walvis Ridge. These percentages are lower than those found by *Froyland et al.* [2015] and *Wang et al.* [2016], but the difference can be mostly explained by the depth variation in eddy volume, which was not considered in those studies.

The variation of density anomaly at the eddy core indicated that smaller-scale mixing processes also contributed to water exchanges between eddy cores and the surrounding waters. These exchanges occurred throughout the eddy lifetimes independently of volume losses. The ability to identify their occurrence based on the density structure reconstructed from in-situ observations is one of the main advantages of the proposed synergistic approach compared with approaches exclusively based on remote-sensing observations. As opposed to coherent-vortex detection methods [*Wang et al.*, 2015; *Froyland et al.*, 2015; *Wang et al.*, 2016], our detection method cannot distinguish whether the eddies investigated in this study were truly coherent structures. In case they were not, our results indicate that even non-coherent structures can contribute significantly to westward transport in the South Atlantic and, thus, they should be included in studies focusing on cross basin eddy-transport. Indeed, the contribution of incoherent transport due to eddy far-field effects effects has been already recognized and discussed (although, not quantified) in studies based on coherent-vortex detection [e.g. *Wang et al.*, 2016; *Abernathey and Haller*, 2018]. On the other hand, in case they were coherent, our results indicate that even such eddies are not completely impermeable to their surroundings due to mixing-induced exchanges. These exchanges are usually ignored in satellite-based transport studies. Assessing their importance relative to the exchanges due to volume loss would help clarify the accuracy of such an assumption. Unfortunately, the reconstructed sections of density cannot be used for quantifying mixing-induced exchanges. Sections of temperature and salinity would be needed, instead, which would require further modifications and testing of the proposed approach. Nonetheless, such an approach would also enable one to quantify the exchanges of heat and salt, key variables to further assess the impact of the transport associated with Agulhas rings and the contribution of Agulhas water in modulating the stratification of the South Atlantic ocean [*Weijer et al.*, 2002].

Another frequent assumption of satellite-based eddy transport studies is to consider the eddies to be uniformly coherent with depth. Our analysis indicates that such an assumption in the South Atlantic is valid between the Walvis and Mid-Atlantic ridges, as well as after the Mid Atlantic Ridge, where the eddies showed their smallest volume variations. However, it might not be as accurate during eddy dissipation, when eddies can show no variations of their characteristics in the first few hundreds meters, while rapidly losing coherence at depth. Our study also shows that the westward transport of warmer and saltier water from eddies *AN1* and *AS2* did not stop after their merging. Eddy *B12* contributed to the further transport of half of the volume from the two eddies beyond the Mid-Atlantic Ridge to the western edge of the basin. Additional westward transport due to coherent eddies formed by the merging of rings from the Agulhas region are usually not considered in eddy transport studies based on coherent-vortex detection [e.g. *Wang et al.*, 2015; *Froyland et al.*, 2015]. Thus, the resulting contribution of coherent eddies to the westward transport across the South Atlantic basin can be potentially underestimated in both volume and areal extent.

Statistical estimates of global eddy transport obtained by combining Eulerian eddy detection and in-situ observations [*Dong et al.*, 2014; *Zhang et al.*, 2014] have been recently questioned for being too large by a new statistical analysis of eddy transport in the Eastern Pacific based on rotationally coherent Lagrangian vortices [*Abernathey and Haller*, 2018]. Two main factors can contribute to such overestimates: an excessive detection of incoherent eddies (hence not associated with mass transport) and an inaccurate reconstruction of the eddy structure and boundaries based on in-situ observations. Since our study focussed on few specific eddies (rather than on a statistical characterization involving a much larger number of eddies over broader spatial and temporal scales), it was possible for us to directly assess both factors in our analysis. Argo profiles within the eddies showed that their cores were characterized by temperature and salinity anomalies that propagated with the eddies, providing in-situ evidence that the eddies trapped and transported eastern South Atlantic water to the western part of the basin over a time-span of roughly 3 years. Regarding the accuracy of the 3D eddy reconstruction, both observations [*van Aken et al.*, 2003] and numerical simulations [*Bettencourt et al.*, 2012] indicate that a radially symmetrical shape with no tilt in the vertical axis is a valid approximations for Agulhas rings (approximately circular eddy boundaries are also detected by coherent-vortex methods, e.g. *Beron Vera et al.* [2013]). The Gaussian profile was also chosen based on the radial distribution of in-situ observations, and the sections that did not show an accurate fit were removed from the analysis. Finally, the resulting eddy radii were consistent with the ones obtained from satellite-based eddy detection (which, compared to other Eulerian methods, also provides more conservative estimates of eddy boundaries [*Nencioli et al.*, 2010]) and were within the range reported in previous studies based on in-situ measurements [e.g. *Casanova-Masjoan et al.*, 2017] as well as satellite-based coherent-vortex detection methods [e.g. *Wang et al.*, 2016]. Future studies in which the different approaches are applied to dedicated numerical model experiments will undoubtedly contribute to better assess the accuracy of the various boundary definitions and the resulting volume estimates for Agulhas rings. More importantly, they might provide insights on possible relationships between the characteristics of rotationally coherent Lagrangian vortices and those of eddies reconstructed from in-situ Argo observations. Such information will be key for further improving the quantification of eddy-induced water transport. While coherent-vortex detection methods are undoubtedly more reliable for identifying eddies associated with water transport, they require integration along a fluid trajectory. Thus, coherent eddies can be detected at the ocean surface from altimetry-derived velocity fields, but not at depth. To date, eddy boundary reconstruction based on hydrographic profiles from the current in-situ observing systems (including Argo floats, AUVs and research vessels) remains, with its limitations, the only available framework for the direct investigation of large-scale eddy-induced transport within the upper thousand meters of the water column.

Altimetry-based Lagrangian experiments showed that water within the eddies was characterized by the highest westward advection rates, further confirming that the eddies are the most efficient process for westward transport across the South Atlantic basin, and consistent with recent numerical model results showing that Agulhas rings can increase the westward propagation of the Agulhas leakage [*Rühs et al.*, 2013]. After eddy *B12* dissipates, the water advected west of 30°W spreads in equal proportions to the north and to the south (~0.25×10^{13} m^3 each) along the Brazilian coast. Water advected to the south is likely to recirculate within the South Atlantic gyre. On the other hand, water advected to the north could potentially enter the North Atlantic [*Lumpkin and Garzoli*, 2005], providing a direct contribution to the surface branch of the South Atlantic meridional overturning circulation (SAMOC). At the same time, west of the Mid-Atlantic Ridge, the majority of Lagrangian particles that escaped the eddies were also advected westward, although at a much slower rate than those within the eddies. Thus, Agulhas water leaked out of the eddies in the western South Atlantic could also potentially reach the Brazilian coast and from there move towards the North Atlantic basin, further enhancing the eddy-induced contribution to the SAMOC. As these results are based on surface currents only, dedicated Lagrangian studies performed at different depths and over longer periods will be needed for a more accurate and exhaustive characterization and quantification of such a contribution.

Our analysis shows that the oxygen anomaly observed by the BGC-Argo float (WMO number 3901496) between 25°W and 30°W was due to the water transport associated with eddy *B12*. Unfortunately, no other BGC-Argo profiles were collected within any of the eddies during their 3-year life cycle. Because of that, it was not possible to couple the volume analysis with a characterization of the biogeochemical properties and transport associated with the eddies. Studies of this type will be possible only after a substantial increase in the density of BGC-Argo observations in the South Atlantic Ocean.

We showed that the approach developed by *Zhang et al.* [2013, 2014] can be successfully adapted and applied to investigate water transport and exchanges associated with specific mesoscale eddies. Our study focused exclusively on the westward transport within the South Atlantic basin, but the origin of the waters initially trapped within eddies *AN1* and *AS2* remain undetermined. Numerical model and satellite-based Lagrangian studies have shown that these waters include contributions from the Indian and the Southern oceans [*Wang et al.*, 2015; *Durgadoo et al.*, 2017]. By further exploiting the synergy between satellite-based Lagrangian experiments and in-situ Argo observations, future studies will be able to better assess the effective contribution of the various water masses to the volume trapped within the eddies formed within the Cape Basin. Another aspect that requires further investigation is how much the characteristics of the observed eddies and their associated transport and exchanges are representative of typical Agulhas rings. This issue could be addressed by extending the analysis over longer time-series and to a larger number of eddies, which would refine estimates of eddy-induced transport of volume (as well as heat and salt) in the South Atlantic Ocean, and of how this transport contributes to the variability of the surface branch of the SAMOC.

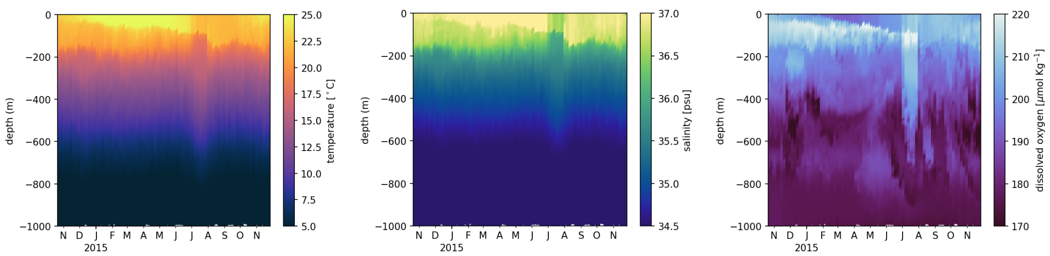

Figure 1. Time series of temperature (left), salinity (middle) and dissolved oxygen profiles (right) collected by the BGC-Argo float between 20 October 2014 and 1 October 2015.

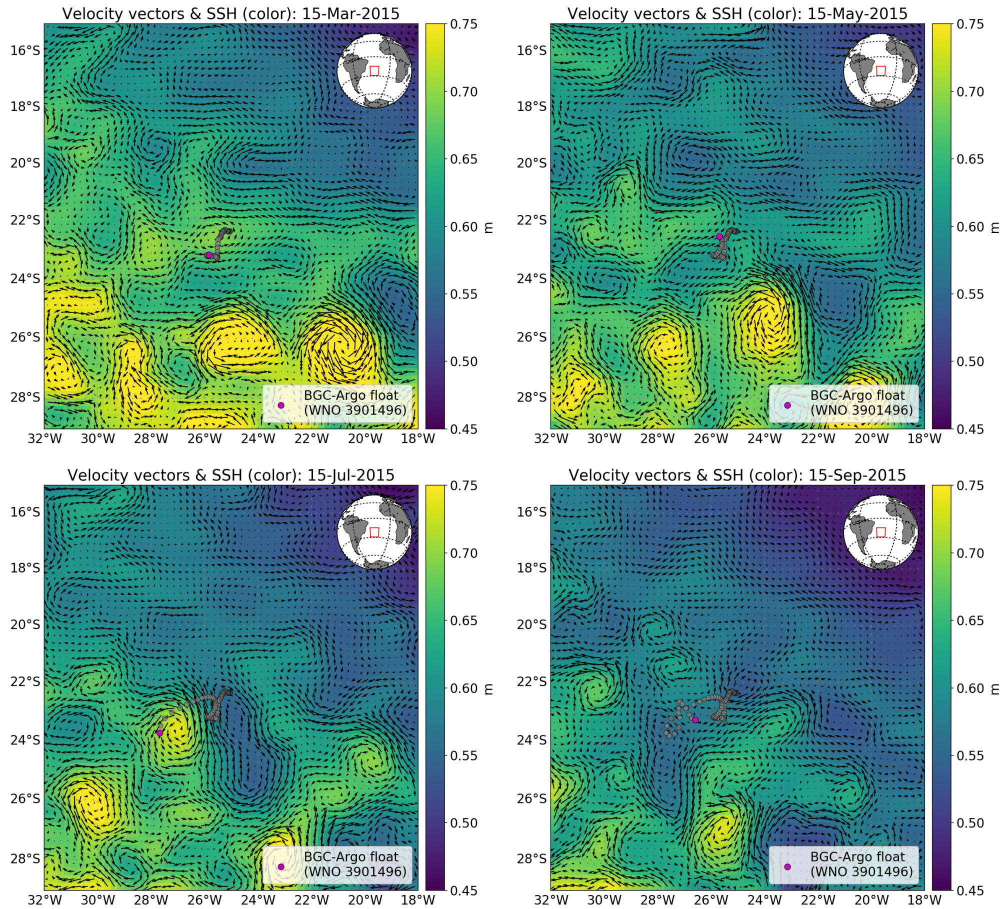

Figure 2. Snapshots of the BGC-Argo float trajectory (gray circles) on 15 March, 15 May, 15 July and 15 September 2015. In each panel, the magenta circle indicates the last position of the float. Sea surface height is shown in colour and the corresponding geostrophic velocities as vectors. A full animation between 20 October 2014 and 1 October 2015 can be seen at https://www.youtube.com/watch?v=nbY6y1z_jAQ .

Appendix

A: Eddy boundary definition

Eddy boundaries were first defined based on closed contours of potential vorticity (PV) as in *Zhang et al.* [2014, 2017]. PV is defined as:

$$PV = \frac{1}{\rho_0} \frac{\partial \rho}{\partial z} (f + \omega) \qquad \text{(A.1)}$$

where f is the Coriolis parameter, ω is the vertical component of relative vorticity and ρ_0 is the mean density. Since we assumed a horizontally uniform background density field, the relative vorticity field $\omega(r, z)$ was computed in cylindrical coordinates as

$$\omega(r, z) = \frac{v(r, z)}{r} + \frac{\partial v(r, z)}{\partial r} = \frac{1}{f\rho_o}\frac{1}{r}\frac{\partial}{\partial r}\left(r\frac{\partial P'(r, z)}{\partial r}\right) \tag{A.2}$$

where $v(r, z) = (f\rho_0)^{-1}\partial P'(r, z)/\partial r$, is the horizontal tangential velocity relative to 2000 m depth obtained from the geostrophic balance. The fields of density anomaly $\rho'_\theta(r, z)$ were also reconstructed from $P'(r, z)$ by inverting the integral from equation 1. Total density was then obtained as $\rho_\theta(r, z) = \rho'_\theta(r, z) + \bar{\rho}_\theta(z)_{Argo}$ and used to compute the 3D fields of vertical density gradient, $\rho_z = \partial\rho_\theta(r, z)/\partial z$.

As $\rho_\theta(r, z)$ was reconstructed from $P'(r, z)$ with depth-varying R_0 and non-analytical $P'_0(z)$, the ρ_z fields were characterized by radial profiles with depth varying width and shape (not always Gaussian), and by alternating patterns of isopycnal stretching and squeezing in the vertical. These patterns were inherited by the PV field, which showed a more complex structure than the three-layer one observed in *Zhang et al.* [2014, 2017], with more alternating layers of local PV maxima and minima. Because of this, vertical profiles of eddy radius based on closed PV contours were particularly noisy with unrealistic sharp transitions from low (<10 km) to high values (>100 km) bounding each layer.

To obtain smoother profiles, we defined eddy boundaries as the largest orbits within closed contours of absolute vorticity, $\eta = (f + \omega)$, instead. Since with a horizontally uniform background density field the orbital planes associated with the eddy are completely horizontal, contours of η were computed relative to each depth level. As f decreases from north to south, closed contours of η were found on a given level only if, on the longitudinal section (i.e. north to south) through the eddy center, values in the southern radial section were larger than the minimum value in the northern one.

Radial profiles of $\omega(r, z)$ (computed as the second radial derivative of the Gaussian function $P'(r, z)$) have usually narrower width than those of $\rho'_\theta(r, z)$ (directly reconstructed from $P'(r, z)$). Therefore, eddy boundaries based on η represent a lower threshold for the actual ones based on PV. Eddy radii are likely underestimated in the upper part of the water column, where density anomalies at the eddy center are large and ρ_z is the leading term determining the radial distribution of PV from equation A.1. However, estimates from η become progressively similar to those from PV at depth, where density anomalies become smaller and ρ_z flatter. Thus, with respect to *Zhang et al.* [2014, 2017], our approach adopted more conservative estimates of eddy dimensions in order to retrieve more accurate estimates of the density vertical structure at the eddy center. The latter is the key variable used in Section 3 for characterizing waters at the eddy cores and investigating mixing-induced cross-eddy exchanges.

Acknowledgments

This study was supported by the UK Natural Environment Research Council National Capability funding to the Plymouth Marine Laboratory. Support from the UK National Centre for Earth Observation is also acknowledged. Argo data were collected and made freely available by the International Argo Program and the national programs that contribute to it. (http://www.argo.ucsd.edu, http://argo.jcommops.org). The Argo Program is part of the Global Ocean Observing System. The SSALTO/DUACS dataset is freely distributed by the European Copernicus Marine Environment Monitoring Service (CMEMS; http://marine.copernicus.eu/).

References

Abernathey, R., and G. Haller (2018), Transport by Lagrangian Vortices in the Eastern Pacific, *Journal of Physical Oceanography*, *48*(3), 667–685, doi:10.1175/JPO-D-17-0102.1.

Amores, A., S. Monserrat, and M. Marcos (2013), Vertical structure and temporal evolution of an anticyclonic eddy in the Balearic Sea (Western Mediterranean), *J. Geophys. Res.*, *118*(4), 2097–2106, doi:10.1002/jgrc.20150.

Amores, A., O. Melnichenko, and N. Maximenko (2017), Coherent mesoscale eddies in the North Atlantic subtropical gyre: 3-D structure and transport with application to the salinity maximum, *J. Geophys. Res.*, pp. n/a–n/a, doi:10.1002/2016JC012256.

Argo (2000), Argo float data and metadata from Global Data Assembly Centre (Argo GDAC). SEANOE., doi:10.17882/42182.

Beal, L. M., W. P. M. De Ruijter, A. Biastoch, and R. Zahn (2011), On the role of the Agulhas system in ocean circulation and climate, *Nature*, *472*(7344), 429–436, doi:10.1038/nature09983.

Beron Vera, F. J., Y. Wang, M. J. Olascoaga, G. J. Goni, and G. Haller (2013), Objective Detection of Oceanic Eddies and the Agulhas Leakage, *Journal of Physical Oceanography*, *43*(7), 1426–1438, doi:10.1175/JPO-D-12-0171.1.

Bettencourt, J. a. H., C. López, and E. Hernández-García (2012), Oceanic three-dimensional Lagrangian coherent structures: A study of a mesoscale eddy in the Benguela upwelling region, *Ocean Model.*, *51*(0), 73 – 83, doi:

10.1016/j.ocemod.2012.04.004.

Boebel, O., J. Lutjeharms, C. Schmid, W. Zenk, T. Rossby, and C. Barron (2003), The Cape Cauldron: a regime of turbulent inter-ocean exchange, *Deep Sea Res. II*, *50*(1), 57 – 86, doi:http://dx.doi.org/10.1016/S0967-0645(02)00379-X, inter-ocean exchange around southern Africa.

Branch, M. A., T. F. Coleman, and Y. Li (1999), A Subspace, Interior, and Conjugate Gradient Method for Large-Scale Bound-Constrained Minimization Problems, *SIAM Journal on Scientific Computing*, *21*(1), 1–23, doi:10.1137/S1064827595289108.

Casanova-Masjoan, M., J. L. Pelegrí, P. Sangrà, A. Martínez, D. Grisolía-Santos, M. D. Pérez-Hernández, and A. Hernández Guerra (2017), Characteristics and evolution of an Agulhas Ring, *J. Geophys. Res.*, pp. n/a–n/a, doi:10.1002/2017JC012969.

Chaigneau, A., A. Gizolme, and C. Grados (2008), Mesoscale eddies off Peru in altimeter records: Identification algorithms and eddy spatio-temporal patterns, *Prog. Oceanogr.*, *79*(2-4), 106–119, doi:10.1016/j.pocean.2008.10.013.

Chaigneau, A., M. Le Texier, G. Eldin, C. Grados, and O. Pizarro (2011), Vertical structure of mesoscale eddies in the eastern South Pacific Ocean: A composite analysis from altimetry and Argo profiling floats, *J. Geophys. Res.*, *116*(C11), C11,025–, doi: 10.1029/2011JC007134.

Chelton, D. B., M. G. Schlax, and R. M. Samelson (2011), Global observations of nonlinear mesoscale eddies, *Prog. Oceanogr.*, *91*(2), 167 – 216, doi: 10.1016/j.pocean.2011.01.002.

de Boyer Montégut, C., G. Madec, A. S. Fischer, A. Lazar, and D. Iudicone (2004), Mixed layer depth over the global ocean: An examination of profile data and a profile-based climatology, *J. Geophys. Res.*, *109*(C12), n/a–n/a, doi:10.1029/2004JC002378, c12003.

De Rutijer, W. P. M., A. Biastoch, S. S. Drijfhout, J. R. E. Lutjeharms, R. Matano, T. Pichevin, P. J. van Leeuwen, and W. Weijer (1999), Indian-atlantic inter–ocean exchange: Dynamics, estimation and impact, *J. Geophys. Res.*, *104*, 20,885–20,910.

de Steur, L., and P. van Leeuwen (2009), The influence of bottom topography on the decay of modeled Agulhas rings, *Deep Sea Res. I*, *56*(4), 471 – 494, doi: 10.1016/j.dsr.2008.11.009.

Doglioli, A. M., B. Blanke, S. Speich, and G. Lapeyre (2007), Tracking coherent structures in a regional ocean model with wavelet analysis: Application to Cape Basin eddies, *J. Geophys. Res.*, *112*(C5), C05043, doi:10.1029/2006JC003952.

Dong, C., J. C. McWilliams, Y. Liu, and D. Chen (2014), Global heat and salt transports by eddy movement, *Nat. Commun.*, *5*, –, doi:10.1038/ncomms4294.

d'Ovidio, F., A. Della Penna, T. W. Trull, F. Nencioli, M.-I. Pujol, M.-H. Rio, Y.-H. Park, C. Cotté, M. Zhou, and S. Blain (2015), The biogeochemical structuring role of horizontal stirring: Lagrangian perspectives on iron delivery downstream of the Kerguelen Plateau, *Biogeosciences*, *12*(19), 5567–5581, doi:10.5194/bg-12-5567-2015.

Durgadoo, J. V., S. Rühs, A. Biastoch, and C. W. Böning (2017), Indian Ocean sources of Agulhas leakage, *J. Geophys. Res.*, pp. n/a–n/a, doi:10.1002/2016JC012676.

Frenger, I., M. Münnich, N. Gruber, and R. Knutti (2015), Southern Ocean eddy phenomenology, *J. Geophys. Res.*, *120*(11), 7413–7449, doi:10.1002/2015JC011047.

Fritsch, F. N., and R. E. Carlson (1980), Monotone Piecewise Cubic Interpolation, *SIAM Journal on Numerical Analysis*, *17*(2), 238–246, doi:10.1137/0717021.

Froyland, G., C. Horenkamp, V. Rossi, and E. van Sebille (2015), Studying an Agulhas ring's long-term pathway and decay with finite-time coherent sets, *Chaos*, *25*(8), 083119, doi:10.1063/1.4927830.

Goni, G. J., S. L. Garzoli, A. J. Roubicek, D. B. Olson, and O. B. Brown (1997), Agulhas ring dynamics from TOPEX/POSEIDON satellite altimeter data, *J. Mar. Res.*, *55*, 861–883.

Gordon, A. L., and W. F. Haxby (1990), Agulhas eddies invade the South Atlantic: Evidence from Geosat altimeter and shipboard conductivity-temperature-depth survey, *J. Geophys. Res.*, *95*, 3177–3125.

Gray, A. R., and S. C. Riser (2014), A Global Analysis of Sverdrup Balance Using Absolute Geostrophic Velocities from Argo, *J. Phys. Oceanogr.*, *44*(4), 1213–1229, doi:10.1175/JPO-D-12-0206.1.

Haller, G., and F. J. Beron-Vera (2013), Coherent Lagrangian vortices: The black holes of turbulence, *J. Fluid Mech.*, *731*, R4, doi:10.1017/jfm.2013.391.

Haller, G., and F. J. Beron-Vera (2014), Addendum to "Coherent Lagrangian vortices: The black holes of turbulence", *J. Fluid Mech.*, *755*, R3, doi:10.1017/jfm.2014.441.

Lehahn, Y., F. d'Ovidio, M. Lévy, Y. Amitai, and E. Heifetz (2011), Long range transport of a quasi isolated chlorophyll patch by an Agulhas ring, *Geophys. Res. Lett.*, *38*(16), L16,610–, doi:10.1029/2011GL048588.

Liu, Y., C. Dong, Y. Guan, D. Chen, J. McWilliams, and F. Nencioli (2012), Eddy analysis in the subtropical zonal band of the North Pacific Ocean, *Deep Sea Res. I*, *68*(0), 54

– 67, doi:10.1016/j.dsr.2012.06.001.

Lumpkin, R., and S. L. Garzoli (2005), Near-surface circulation in the Tropical Atlantic Ocean, *Deep Sea Res. I*, *52*(3), 495 – 518, doi:10.1016/j.dsr.2004.09.001.

Lyman, J. M., and G. C. Johnson (2015), Anomalous eddy heat and freshwater transport in the Gulf of Alaska, *J. Geophys. Res.*, *120*, 1397–1408, doi:10.1002/2014JC010252.

McDougall, T. J., and O. A. Krzysik (2015), Spiciness, *Journal of Marine Research*, *73*(5), 141–152, doi:doi:10.1357/002224015816665589.

Nencioli, F., C. Dong, T. Dickey, L. Washburn, and J. C. McWilliams (2010), A Vector Geometry-Based Eddy Detection Algorithm and Its Application to a High-Resolution Numerical Model Product and High-Frequency Radar Surface Velocities in the Southern California Bight, *J. Atmos. Ocean. Tech.*, *27*(3), 564–579, doi:10.1175/2009JTECHO725.1.

Nencioli, F., F. d'Ovidio, A. M. Doglioli, and A. A. Petrenko (2011), Surface coastal circulation patterns by in-situ detection of Lagrangian coherent structures, *Geophys. Res. Lett.*, *38*(17), L17,604, doi:10.1029/2011GL048815.

Olson, D. B. (1991), Rings in the ocean, *Annu. Rev. Earth Planet. Sci.*, *19*(1), 283–311, doi:10.1146/annurev.ea.19.050191.001435.

Qiu, B., and S. Chen (2005), Eddy-Induced Heat Transport in the Subtropical North Pacific from Argo, TMI, and Altimetry Measurements, *J. Phys. Oceanogr.*, *35*(4), 458–473, doi:10.1175/JPO2696.1.

Rühs, S., J. V. Durgadoo, E. Behrens, and A. Biastoch (2013), Advective timescales and pathways of Agulhas leakage, *Geophys. Res. Lett.*, *40*(15), 3997–4000, doi:10.1002/grl.50782.

Schouten, M. W., W. P. M. de Ruijter, P. J. van Leeuwen, and J. R. E. Lutjeharms (2000), Translation, decay and splitting of Agulhas rings in the southeastern Atlantic Ocean, *J. Geophys. Res.*, *105*(C9), 21,913–21,925, doi:10.1029/1999JC000046.

Souza, J. M. A. C., C. de Boyer MontÃĺgut, C. Cabanes, and P. Klein (2011), Estimation of the Agulhas ring impacts on meridional heat fluxes and transport using ARGO floats and satellite data, *Geophys. Res. Lett.*, *38*(21), L21,602–, doi:10.1029/2011GL049359.

SSALTO/DUACS User Handbook (2016), *(M)SLA and (M)ADT Near-Real Time and Delayed Time Products*, cLS-DOS-NT-06-034.

van Aken, H., A. van Veldhoven, C. Veth, W. de Ruijter, P. van Leeuwen, S. Drijfhout, C. Whittle, and M. Rouault (2003), Observations of a young Agulhas ring, Astrid, during MARE in March 2000, *Deep Sea Res. II*, *50*(1), 167–195, doi:10.1016/S0967-0645(02)00383-1.

van Sebille, E., P. J. van Leeuwen, A. Biastoch, and W. P. M. de Ruijter (2010), On the fast decay of Agulhas rings, *J. Geophys. Res.*, *115*(C3), n/a–n/a, doi: 10.1029/2009JC005585, c03010.

van Sebille, E., S. M. Griffies, R. Abernathey, T. P. Adams, P. Berloff, A. Biastoch, B. Blanke, E. P. Chassignet, Y. Cheng, C. J. Cotter, E. Deleersnijder, K. Döös, H. Drake, S. Drijfhout, Gary Stefan F., A. W. Heemink, J. Kjellsson, I. M. Koszalka, M. Lange, C. Lique, G. A. MacGilchrist, R. Marsh, C. G. Mayorga-Adame, R. McAdam, F. Nencioli, C. B. Paris, M. D. Piggott, J. A. Polton, S. Rühs, S. H. Shah, M. D. Thomas, J. Wang, P. J. Wolfram, L. Zanna, and J. D. Zika (2018), Lagrangian ocean analysis: fundamentals and practices, *Ocean Modelling*, *121*, 49–75, doi:10.1016/j.ocemod.2017.11.008.

Wang, Y., M. J. Olascoaga, and F. J. Beron Vera (2015), Coherent water transport across the South Atlantic, *Geophys. Res. Lett.*, pp. n/a–n/a, doi:10.1002/2015GL064089, 2015GL064089.

Wang, Y., F. J. Beron-Vera, and M. J. Olascoaga (2016), The life cycle of a coherent Lagrangian Agulhas ring, *J. Geophys. Res.*, *121*(6), 3944–3954, doi: 10.1002/2015JC011620.

Weijer, W., W. P. De Ruijter, A. Sterl, and S. S. Drijfhout (2002), Response of the atlantic overturning circulation to south atlantic sources of buoyancy, *Global and Planetary Change*, *34*(3), 293 – 311, doi:10.1016/S0921-8181(02)00121-2.

Zhang, Z., Y. Zhang, W. Wang, and R. X. Huang (2013), Universal structure of mesoscale eddies in the ocean, *Geophys. Res. Lett.*, *40*(14), 3677–3681, doi:10.1002/grl.50736.

Zhang, Z., W. Wang, and B. Qiu (2014), Oceanic mass transport by mesoscale eddies, *Science*, *345*(6194), 322–324, doi:10.1126/science.1252418.

Zhang, Z., Y. Zhang, and W. Wang (2017), Three-compartment structure of subsurface-intensified mesoscale eddies in the ocean, *J. Geophys. Res.*, pp. n/a–n/a, doi: 10.1002/2016JC012376.

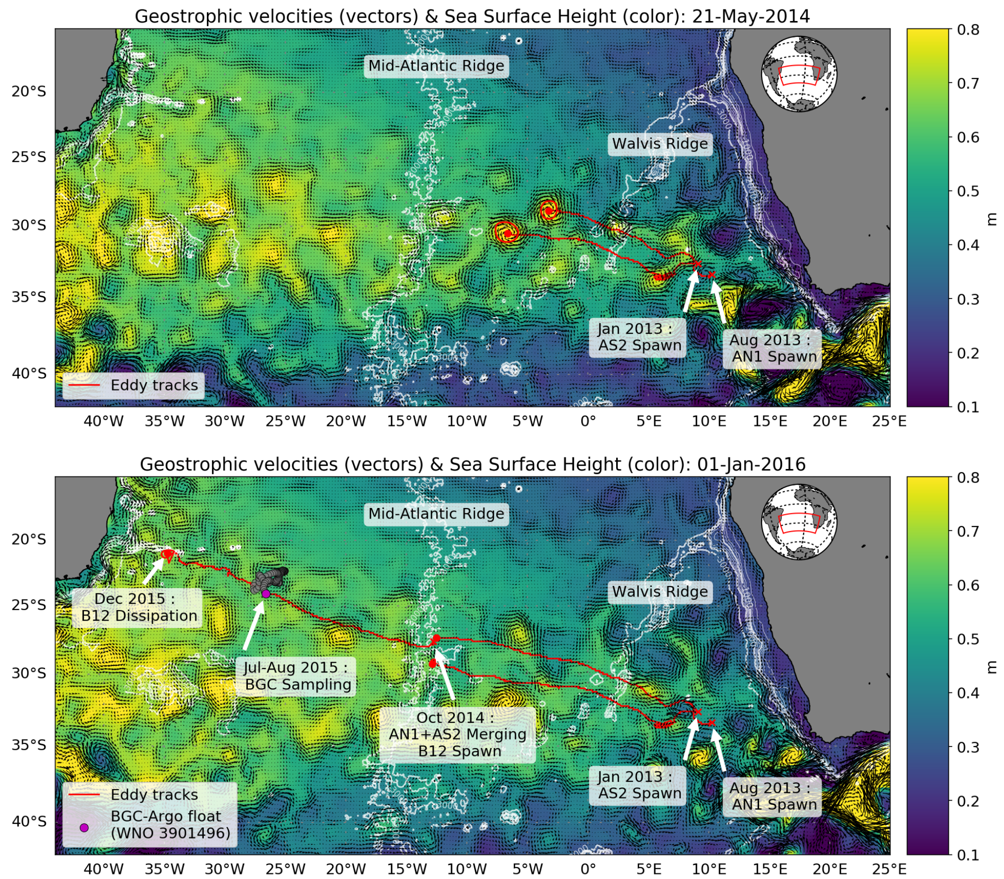

Figure 3. (Top) Tracks of eddies *AN1* and *AS2* (in red) from 1 January 2013 to 21 May 2014. Eddy boundaries on 21 May 2014 are also indicated. Sea surface height is shown in colour and the corresponding geostrophic velocities as vectors. Bathymetric contours are shown in white, with the two main ridges explicitly labelled. White text boxes and arrows mark the times and locations of key events along the eddy tracks. (Bottom) Same as top panel, but until 1 January 2016. Eddy *B12* spawned by the merging of eddies *AN1* and *AS2* west of 10°W. The boundary of eddy *B12* on 29 December 2015 (last day the eddy was detected) are also indicated. The trajectory of the BGC-Argo float is shown by gray circles. A full animation between 1 January 2013 and 31 March 2016 can be seen at https://www.youtube.com/watch?v=8vSvwMql61k
.

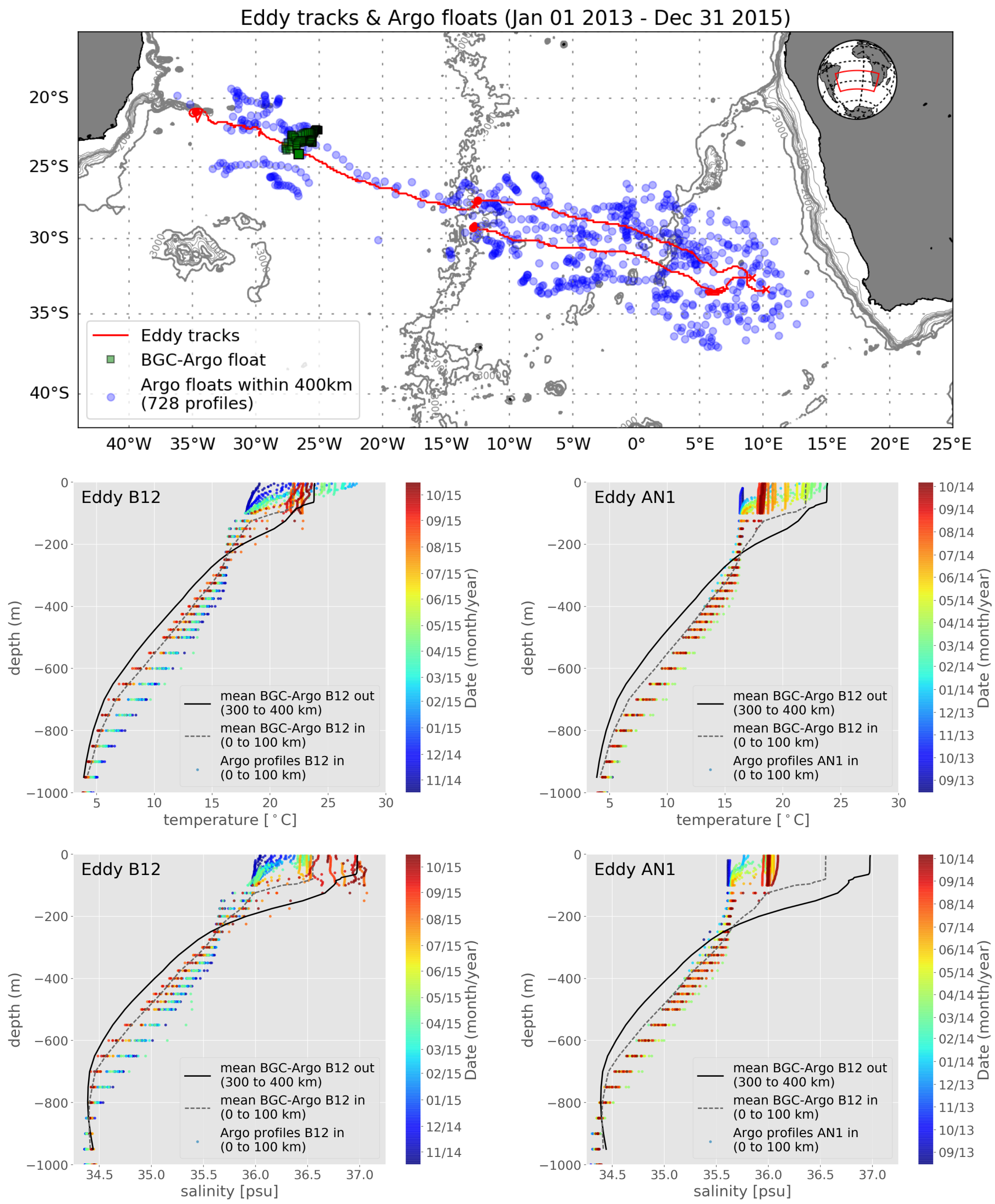

Figure 4. (Top) Tracks of eddies *AN1*, *AS2* and *B12* (red lines). Position of the Argo profiles collected within 400 km from the centers of the eddies between 1 January 2013 and 31 December 2015 (blue circles). Position of the profiles collected by the BGC-Argo float between October 2014 and November 2015 (green squares). (Middle and Bottom) Argo profiles of conservative temperature and absolute salinity collected within 100 km of the centers of eddy *AN1* and *B12* (right and left, respectively). The profiles have been interpolated to the depths of the WOA 2013. The dashed gray lines represent the average profiles observed by the BGC-Argo float within eddy *B12*. The solid black lines represent the average profiles observed by the same float between 300 and 400 km from the center of eddy *B12*.

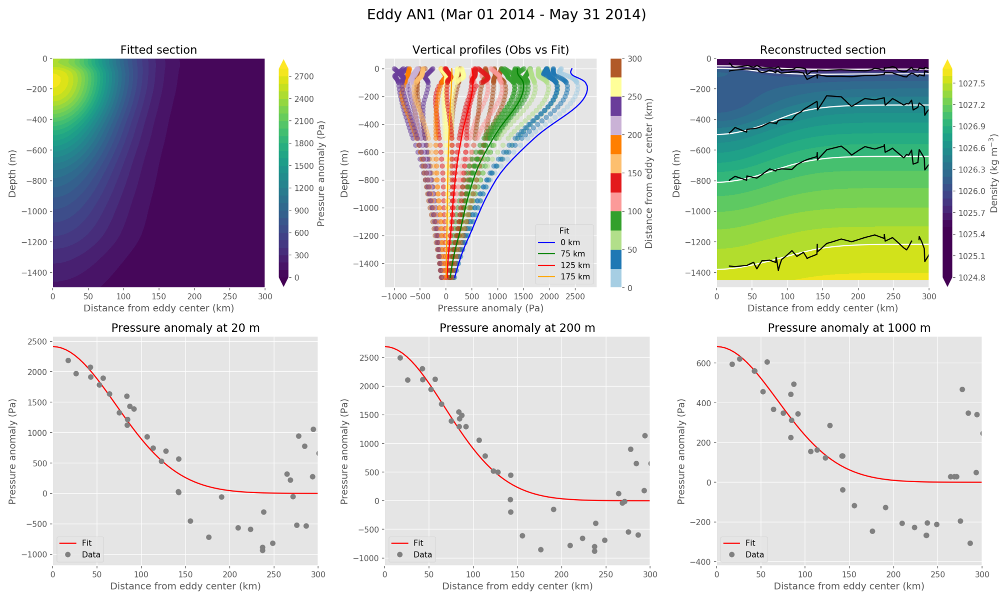

Figure 5. (Top left) Vertical section of reconstructed pressure anomaly for eddy *AN1* on April 2014. (Top center) Vertical profiles of pressure anomaly from Argo observations (circles) and from the reconstructed section (solid lines) at various distances from the eddy center. (Top right) Reconstructed vertical section of density. White contours are densities 1025.5, 1026.0, 1026.5, 1027.0 and 1027.5 kg m^{-3}. Black contours are the same densities, but from Argo observations. (Bottom) Radial distribution of pressure anomaly from Argo observations (circles) and reconstructed Gaussian radial sections (red line) for depths of 20, 200 and 1000 m. The fit was based on the Argo observations (38 profiles within 300 km from the eddy center) collected between 1 March 2014 and 31 May 2014.

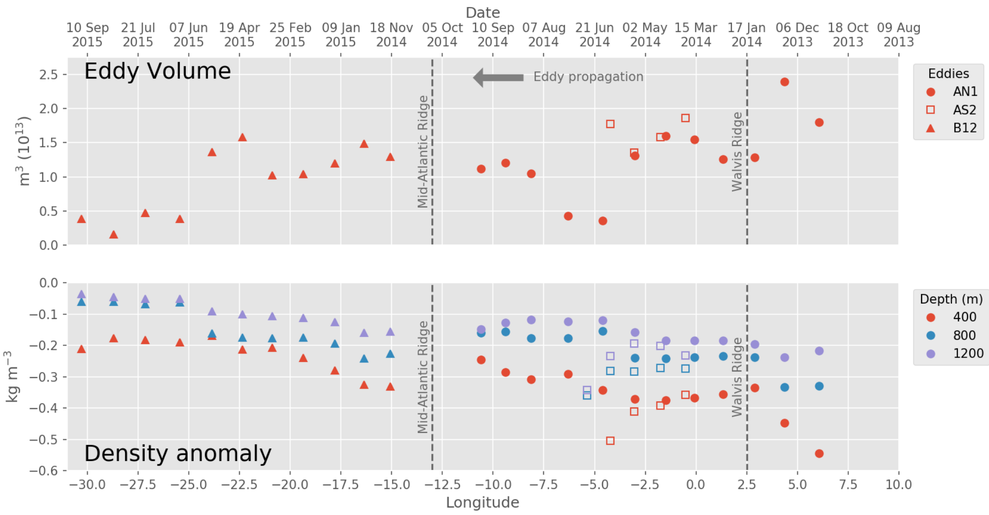

Figure 6. Time series of reconstructed eddy volume from 0 to 1500 m depth (top) and density anomaly at the eddy center (bottom) for the three eddies. The anomalies are all relative to the background profile from September 2015, the last month in which the structure of eddy *B12* was reconstructed. Different symbols represent different eddies; different colours represent different depths. Data are plotted with respect to their latitudinal position for easier comparison with the maps in figures 4 and 7. The dates in the top panel correspond to the days on which eddies *AN1* and *B12* were observed at those longitudes, providing a temporal reference frame for the interpretation of the time series.

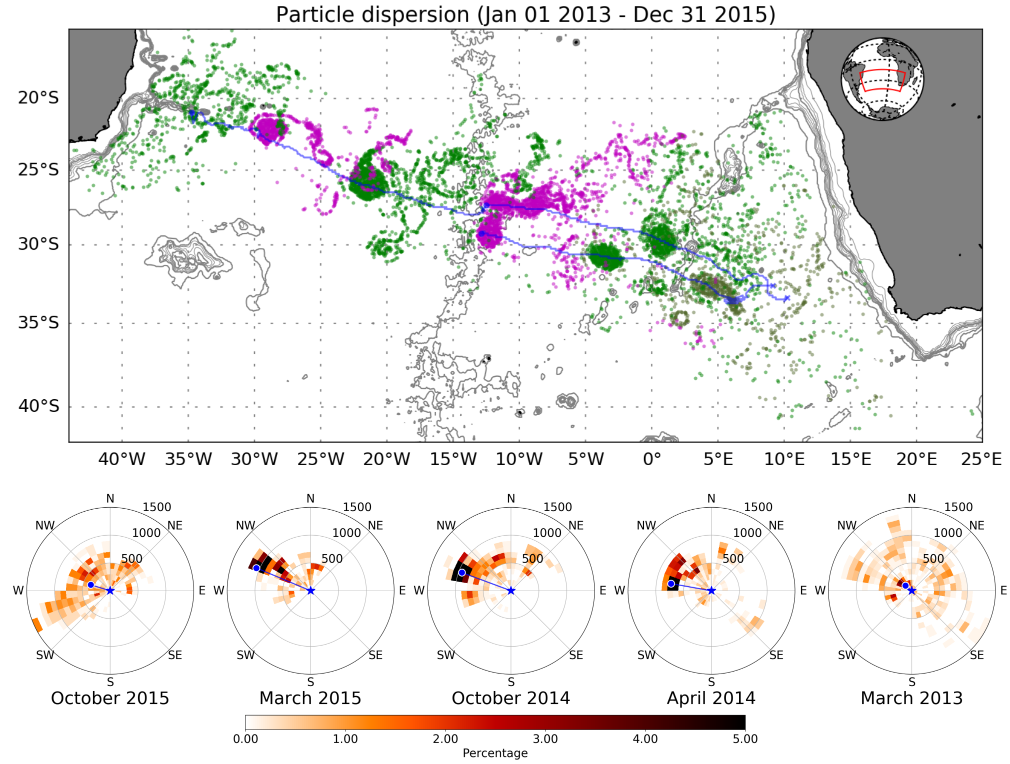

Figure 7. (Top) Dispersion patterns after six months of advection for the particles released within 150 km from the eddy centers on March 2013, September 2013, April 2014, October 2014, March 2015 and October 2015, respectively. Particles for the first two releases are shown in different shades of green. Particles from subsequent releases are shown in alternating magenta and green. Eddy tracks are shown in blue. A full animation of all Lagrangian experiments can be seen at https://www.youtube.com/watch?v=_WkTloTrxUQ . (Bottom) Polar distribution of particle dispersion for all releases from the top panel except September 2013 (analogous dispersion pattern as March 2013). The three rightmost panel are relative to eddy *AS2*; the two leftmost to eddy *B12*. The blue circles indicate the position of the eddy center with respect to its initial position 180 days earlier represented by the blue star at the center of each panel. Radial distance in each panel is in km.